Journal of Alloys and Compounds 801 (2019) 409–414

Contents lists available at ScienceDirect

Journal of Alloys and Compounds

journal homepage: http://www.elsevier.com/locate/jalcom

Opto-electronic properties of Co-Zn-Ni-O films deposited by RF-sputtering at ambient-temperature

J.C. Ford [a, b], A. Zakutayev [a], P.F. Ndione [a], A.K. Sigdel [a, c], N.E. Widjonarko [a, b], P.A. Parilla [a], B. Van Zeghbroeck [b], J.J. Berry [a], D.S. Ginley [a], J.D. Perkins [a, *]

[a] National Renewable Energy Laboratories, Golden, CO 80401, USA
[b] University of Colorado Boulder, Boulder, CO 80309, USA
[c] University of Denver, Denver, CO 80210, USA

ARTICLE INFO

Article history:
Received 21 January 2018
Received in revised form
16 May 2019
Accepted 23 May 2019
Available online 24 May 2019

Keywords:
Oxide materials
Thin films
Vapor deposition
Electrical transport
Optical properties
Crystal structure

ABSTRACT

Co-Zn-Ni-O thin films were grown on glass at ambient temperature ($T_S < 65$ °C) by co-sputtering from Co_3O_4, ZnO, and NiO targets to determine the structural and opto-electronic properties across the ternary composition space. Compositional domains with spinel, wurtzite, rock-salt, and mixed phases were observed, albeit with very weak X-ray diffraction peaks, overall suggesting the likely presence of a co-existent amorphous component. The electrical conductivity had a maximum value of ~35 S/cm that occurs where the optical absorption is also the strongest. The work functions range from 5.0 to 5.8 eV for all samples, but with no clear composition-based trends. Overall, it appears that the optoelectronic properties of the Co-Zn-Ni-O materials are much less sensitive to substrate temperature compared to other p-type oxide semiconductors, resulting in technologically-relevant ambient-temperature-deposited thin films.

1. Introduction

The crystalline mixed-cation spinels M_2ZnO_4 (M = Ir, Rh, Co) are known p-type oxide semiconductors with a normal spinel structure and optical band gaps ranging from 2 to 3 eV [1,2]. The realization in 2003 of an all-oxide p-n diode using p-type amorphous $ZnO \cdot Rh_2O_3$ [3] demonstrated that this general class of materials could be used in opto-electronic device applications and that the materials need not be crystalline to be technologically relevant. Subsequent device application work has focused primarily on the related, and much less expensive, Co-based materials Co_2ZnO_4 (a normal spinel) and Co_2NiO_4 (an inverse spinel). Specifically, ambient-temperature-deposited and usually amorphous Co-Zn-O and Co-Ni-O have been used as p-type materials in diodes [4] and transistors [5,6], and, due to their high work function (~5–6 eV [7]), as hole transport layers (HTLs) for organic photovoltaics [7,8] and dye-sensitized solar cells [9]. In addition, crystalline Co_2ZnO_4 [10] and Co_2NiO_4 [11] have been used as catalytic electrodes for the oxygen evolution reaction in photo-electrochemical splitting of water.

The application work has generally used ambient-temperature-deposited materials; however, the material science work, to date, has largely focused on crystalline materials grown at elevated temperatures (200°–600 °C). Beginning from the parent material Co_3O_4, phase-pure and highly crystalline spinel $Co_{3-x}Zn_xO_4$ is easily grown by sputtering or pulsed laser deposition for all compositions between Co_3O_4 (x = 0) and Co_2ZnO_4 (x = 1) [7,12]. Due to the non-equilibrium nature of these physical vapor deposition (PVD) methods, additional Zn beyond x = 1 can be incorporated up to $x \approx 1.6$ for films grown at $T_S = 300$ °C [7]. At higher temperatures, less additional Zn can be incorporated. For any given deposition temperature, the electrical conductivity of $Co_{3-x}Zn_xO_4$ generally increases with increasing Zn incorporation up to the limit of ZnO phase separation [7,13] because the substitution of Zn onto an octahedral Co site is an acceptor dopant in this material [13,14].

Similarly, for $Co_{3-x}Ni_xO_4$, equilibrium materials growth methods find that Ni can be incorporated up to Co_2NiO_4 (x = 1) [15], whereas using non-equilibrium thin-film growth methods, additional Ni can be incorporated without NiO precipitation up to about $Co_{1.5}Ni_{1.5}O_4$ (x = 1.5) [7,15–17]. Also, like Co-Zn-O, for Co-Ni-O, the electrical conductivity increases with increasing Ni with a maximum conductivity $\sigma \approx 200$ S/cm for as-grown sputtered films deposited at

* Corresponding author.
E-mail address: john.perkins@nrel.gov (J.D. Perkins).

https://doi.org/10.1016/j.jallcom.2019.05.275

$T_S \approx 300\,^{\circ}C$ [7] and $\sigma \approx 375$ S/cm for ambient-temperature-sputtered films that were subsequently annealed in air at 375 °C [17,18]. Further, for $Co_{3-x}Ni_xO_4$, the conductivity depends strongly on the oxygen partial pressure during film growth [8,17].

The more general Co-Zn-Ni-O pseudo-ternary composition space has been explored using sputtering-based, high-throughput, composition-gradient combinatorial methods, albeit at a fixed $T_S = 350\,^{\circ}C$ and fixed $pO_2 = 10$ mT [19]. Focusing on the composition-dependent trends in this ternary cation system, the highest conductivity, $\sigma \approx 100$ S/cm, occurs in an area centered at Co_2NiO_4, but the best combination of high conductivity and low optical absorption occurs closer to $Co_{1.7}Ni_{0.8}Zn_{0.5}O_4$ [19], a composition that would be difficult to guess from the prior pseudo-binary Co-Zn-O and Co-Ni-O studies. However, no similar materials information is currently available for pseudo-ternary Co-Zn-Ni-O films deposited at ambient temperature, which, as discussed above, are more commonly used for applications [4–8].

To address this lack of more application-relevant materials data, Co-Zn-Ni-O thin films were deposited onto ambient-temperature glass substrates by RF sputtering with $pO_2 = 10$ mT. Three sputter sources (ZnO, NiO, and Co_3O_4) were used in an off-axis co-sputtering configuration to create combinatorial libraries with intentional compositional gradients. The crystal structure, conductivity, transparency, and work function were measured as a function of the measured composition across the majority of the pseudo-ternary composition space. For the ambient-temperature-deposited Co-Zn-Ni-O films, the conductivity ranged from 0.004 to 35 S/cm and the optical absorption coefficient (α) at $\hbar\omega = 1.8$ eV ($\lambda = 700$ nm) ranged from 1×10^4 to 2×10^5 cm^{-1}. Additionally, for all compositions, the Kelvin-probe-measured work function (ϕ) lay between 5.0 and 5.8 eV, but there were no clear trends with composition. The maximum conductivity and maximum optical absorption both occur in a narrow composition region on the Co_3O_4–NiO tie line between Co_2NiO_4 and NiO, where the films are the least crystalline. All of the data for this study, including deposition details, is available through the NREL High Throughput Experimental Materials Database (HTEM DB, https://htem.nrel.gov see Supplemental Information for details) [22] with the exception of the two grazing incidence x-ray diffraction (XRD) measurements.

Overall, the optical absorption and work function for these ambient-temperature-deposited Co-Zn-Ni-O films are similar to those for films grown at 350 °C [19]. However, the maximum conductivity decreases by a factor of three from $\sigma = 110$ S/cm for $T_S = 350\,^{\circ}C$ to $\sigma = 35$ S/cm for the films grown at ambient temperature, with all other parameters the same [19]. We note that this decrease in conductivity is much smaller than the factor of 10^3 observed for p-type delafossite ($CuAlO_2$ family) thin films [20,21]. This relative deposition-temperature insensitivity of the electrical conductivity in Co-Zn-Ni-O materials may be because the low-energy cation anti-site defects in Co_2ZnO_4 and similar spinels are not detrimental, but rather, are actually net acceptor doping defects [13,14]. Accordingly, we find that ambient-temperature-deposited Co-Zn-Ni-O thin-film materials have promising opto-electronic properties for device applications provided that high transparency is not need or that very thin layers can be used, such as for HTLs.

2. Experimental methods

The Co-Zn-Ni-O films were grown by co-sputtering in a 1:1 O_2:Ar mixture at 20 mTorr total pressure using RF power. A base pressure of 2.1×10^{-6} Torr or lower was achieved before all depositions. All depositions were conducted at ambient temperatures and the measured substrate temperature, which increased due to plasma heating, did not exceed 65 °C. All films were deposited onto $2'' \times 2''$ Corning Eagle 2000 glass substrates that were ultrasonically cleaned sequentially in acetone and IPA for 15 min followed by a 5-min O_2 plasma reactive-ion etch prior to film deposition. Three 2″-diameter sputter magnetrons (Angstrom Sciences) were positioned off center and oriented at an angle to the substrate to yield intentional two-dimensional composition gradients across each 2″ 2″ sample library. The deposition details for the 17 libraries used in this work are provided in Table S1 of the Supplemental Information. All material property measurements (except for Kelvin probe measurements) were taken on the same 44-point grid so that the measurements could be compared directly.

The film composition was measured with a Matrix Metrologies MaXXi 5 PIN x-ray fluorescence (XRF) system with a tungsten anode, 800-μm collimator, and 300–450-s measurement times. The obtained spectra were analyzed with MTF-FP software to yield cation ratios and film thickness. The XRF-based thickness measurements were calibrated by direct profilometer (Dektak 8) measurements of a reference Zn-Ni-Co-O sample grown at the same conditions. The XRD mapping measurements were performed with a Bruker AXS D8 Discover 8- axis system with a Cu K_α source and a two-dimensional detector using integration times of 300–450 s. The grazing incidence XRD measurements were performed with a Rigaku DMAX diffractometer with a Cu K_α source and a point detector.

The optical transmission and reflection spectra were measured from 300 to 1000 nm with an Ocean Optics CCD array spectrometer coupled to a home-built fiber-optic-based mapping system with a combined deuterium plasma and tungsten-filament light source. The optical absorption coefficient was calculated from the measured transmittance (T), reflectance (R), and film thickness (d) using:

$$\alpha = -\frac{1}{d}\ln\left(\frac{T}{1-R}\right) \quad (1)$$

The sheet resistance (Rs) was measured with a standard co-linear four-point-probe technique using a current of 1 μA. The work-function measurements were made using a scanning Kelvin probe (KP Technologies SKP 450) on a 440-point grid and then spatially averaged to match the 44-point grid used for all other measurements. The samples were kept in air for up to three weeks before the Kelvin probe measurements.

3. Results

3.1. Crystal structure

The representative XRD patterns in Fig. 1(a) show the main phases and some of the mixed phases that were measured across the Co-Zn-Ni-O materials. Representative measured patterns—which include wurtzite (WZ), rock-salt (RS), spinel (SP), and mixed RS + SP —are shown using different colors. Note that measured patterns are normalized by film thickness and integration time to allow a fair comparison of their respective intensities. Fig. 1(b) shows reference patterns for spinel, rock-salt, and wurtzite crystal structures from the simulated ICDD powder diffraction patterns of Co_3O_4, NiO, and ZnO. In one composition region, the background subtracted patterns analyzed here showed no observable crystalline scattering. A representative pattern for this region is shown here in black and labelled 'No detected phase'. The specific composition locations for the five representative XRD patterns are shown in the inset as well as by square markers in Fig. 2.

Notably, the intensity of the XRD peaks for these ambient-temperature-deposited films is much lower than that measured in Ref. [19] for compositionally comparable films grown at

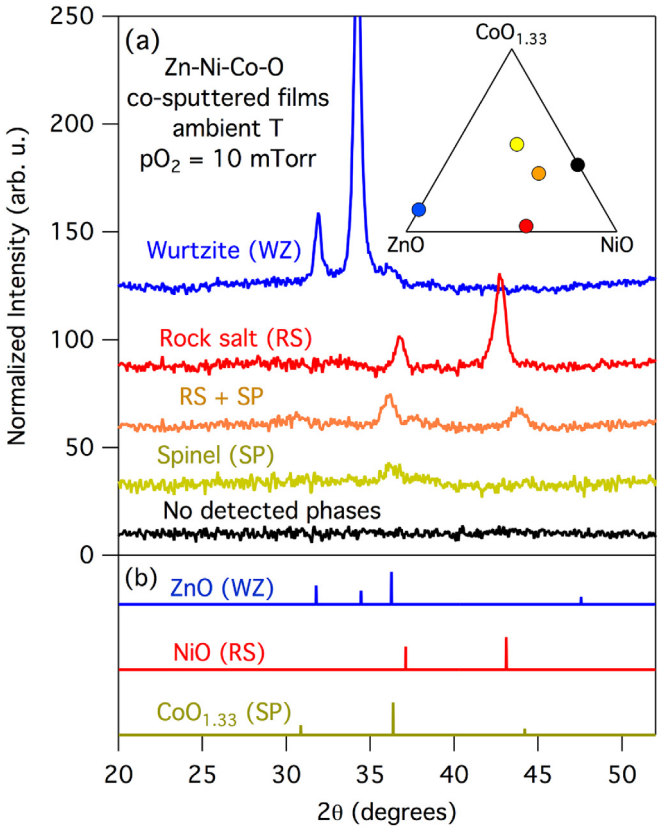

Fig. 1. (a) Representative measured XRD patterns from the different detectable phases observed. (b) Calculated reference spectra for the different structures from the ICDD database. Co_3O_4 (PDF card 00-042-1467), NiO (PDF card 00-044-1159), and ZnO (PDF card 00-036-1451).

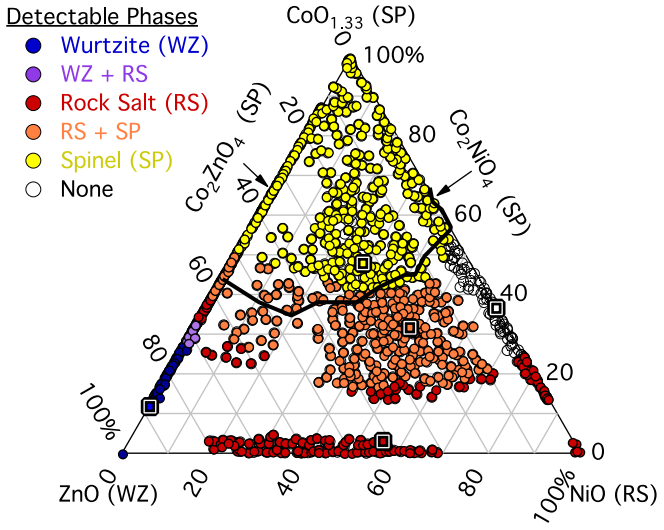

Fig. 2. Regions of different detected phases found in the Co-Zn-Ni-O material system. Overlaid square symbols squares denote the points for the representative XRD patterns displayed in Fig. 1. The solid black line is the phase boundary between the spinel and mixed rock-salt/spinel region for films deposited at 350 °C [19]. The known crystalline phases are labelled: (SP) = Spinel, (WZ) = Wurtzite, and (RS) = Rock-salt.

$T_S = 350$ °C. The peaks are also relatively broad, indicating small grain sizes, crystalline disorder, or nonuniform strain for the crystallites in the films. Overall, the distinct lack of strong XRD peaks suggests that the observed crystalline phases are likely mixed with a substantial amorphous or nano-crystalline component. We note that the automated background subtraction process used for these high-throughput mapping measurements to remove the scattering from the amorphous glass substrate will also remove any amorphous scattering arising from the film. Hence, we cannot quantify an amorphous component. Representative as-measured and background subtracted spectra are shown in Fig. S1 of the Supplemental Information.

The composition regions for the different structures are shown in Fig. 2. Samples that did not have detectable peaks using our laboratory-scale XRD instrument are indicated as 'None'. We emphasize that Fig. 2 is not a phase diagram, but rather, only a map of observed *detectable* phases. As discussed above, given the weak scattering and broad peaks, it is likely the films are mixed phase with an amorphous or nano-crystalline component present in addition to the observed phase for most, if not all, compositions.

Near the vertices of Fig. 2, the samples show the expected crystalline structure. A large area of the composition space extending away from the Co_3O_4 corner has a spinel structure (yellow markers). In the center of the ternary phase space, the separation of spinel and rock-salt-type crystal structures occurs for Co percentages smaller than 40%–55%, as shown in Fig. 2. Mixed rock-salt and spinel structures are present below these Co cation percentages (orange markers). Along the Co_3O_4–ZnO tie line, the observed structure goes with increasing Zn content from spinel to rock-salt to wurtzite with mixed-phase regions in between. The rock-salt phase is observed on the ZnO–Co_3O_4 tie line for Zn percentages from 61% to 66%.

Along the Co_3O_4–NiO tie line, a no-phases-observed region (no detectable XRD peaks in high-throughput mapping measurements) is observed for Co concentrations between 24% and 57%. Here, it is likely that structural frustration between the spinel (Co_2NiO_4) and rock-salt (NiO) phases leads to the formation of this poorly crystalline region for films grown at low (ambient) temperatures [23,24]. This observed region extends only slightly (~6% Zn concentration) into the center of the phase diagram.

Of the representative XRD patterns shown in Fig. 1, those for the spinel region (yellow) and the no-phases region (black) are the hardest to assign a structure, given the very low signal level obtained for the high-throughput mapping measurements with which this data was collected. Accordingly, to better assess the crystalline structure of these regions, we performed grazing incidence ($\omega = 0.425°$) x-ray diffraction measurements (GIXRD) for a library representative of each of these regions. The measured patterns shown in Fig. 3 have clearly observable peaks corresponding to the spinel structure. Due to the substantial spot size broadening inherent to grazing incidence measurements, these two measurements each cover many mapping sample spots shown in Fig. 2, and hence are representative of a region rather than a single composition. Nevertheless, these GIXRD measurements both confirm the observation of a spinel structure in the 'spinel' region of Fig. 2 and demonstrate that the 'no-phases-observed' region is not really amorphous.

3.2. Optoelectronic properties

The conductivity values (calculated from the sheet resistance and thickness measurements) are shown in Fig. 4, plotted versus the ternary composition space. The electrical conductivity generally increases with decreasing Zn content. The lowest conductivities ($\sigma \approx 4.2 \times 10^{-3}$ S/cm) are on the ZnO–Co_3O_4 binary tie line with high Zn concentrations. The maximum conductivity ($\sigma \approx 35$ S/cm) occurs on the Zn-free edge of the ternary composition diagram with Co percentages between 30% and 50% along the Co_3O_4–NiO tie line. We note that there is substantial spread in the measured

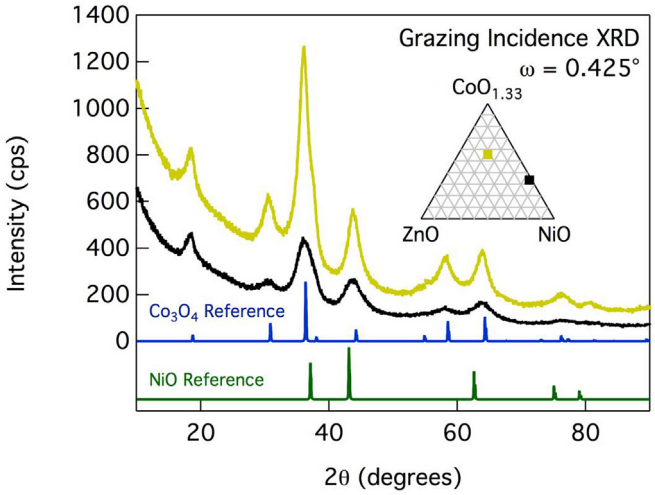

Fig. 3. Measured grazing incidence x-ray diffraction (GIXRD) patterns for representative spots in the Spinel and No-phases-observed regions Fig. 2. Co_3O_4 spinel (blue) and NiO rock salt (green) reference patterns are shown for comparison. The inset shows the central composition of the measured spots.

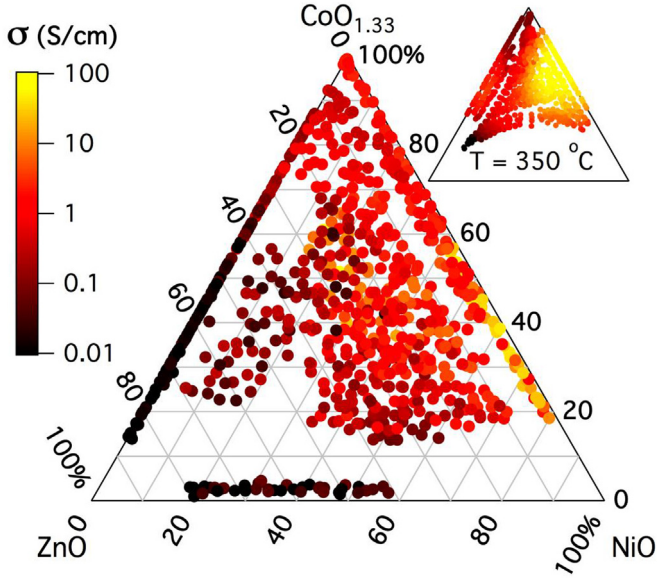

Fig. 4. Electrical conductivity (σ) as a function of metal composition for ambient-temperature depositions. (Inset) Conductivity as a function of composition for depositions at 350 °C [19].

conductivity (color variation in Fig. 4) for compositionally similar samples. Electrical conductivity is very sensitive to small changes in defect concentrations and film morphology with the measured variations in electrical conductivity likely occurring due to the different synthesis conditions used for libraries with compositional overlap. Accordingly, for any given compositional region, the higher conductivity values can be taken as a representative upper bound on the conductivity achievable at ambient temperature in our deposition system.

Optical transmission spectra for four representative films are shown in Fig. 5 with the cation composition for each plotted in the inset. The Zn-rich film ($Zn_{0.88}Co_{0.12}O_y$) which is close to the ZnO corner is ~80% transparent for $\lambda > 700$ nm and shows a semiconductor-like increase in absorption for shorter wavelengths. In contrast, the other three spectra shown all have a low

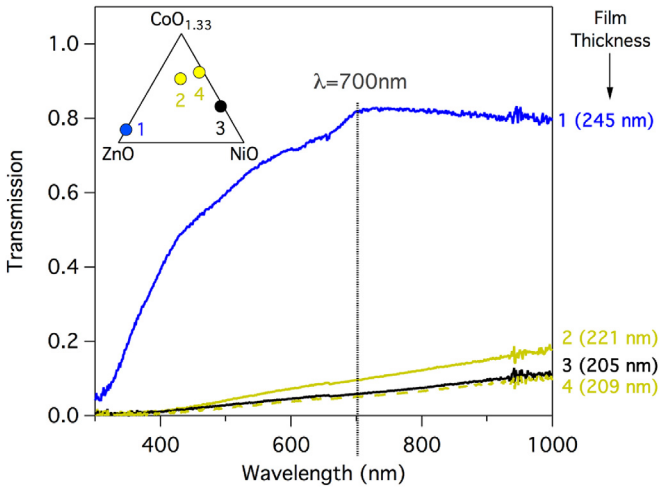

Fig. 5. Optical transmission vs. wavelength spectra for Co-Zn-Ni-O films with different compositions. (Inset) Shows the location in compositional space of the four transmission spectra.

transmission across the entire visible spectrum, with no clear onset of absorption. This includes Spectrum 2, which indicates a ternary-cation film with detectable spinel XRD peaks (see Figs. 1 and 2), as well as Spectrum 3 for a no-phases-observed film from the highest-conductivity region and Spectrum 4 that has a composition very close to Co_2NiO_4.

To provide a thickness-independent view of the optical properties, Fig. 6 shows the absorption coefficient at $\lambda = 700$ nm ($\hbar\omega = 1.8$ eV). The minimum absorption coefficient, $\alpha = 5.7 \times 10^3\ cm^{-1}$, occurs at $Zn_{0.86}Co_{0.14}O_y$, which is close to the ZnO vertex. The maximum value, $\alpha = 2.0 \times 10^5\ cm^{-1}$, occurs at $Co_{0.33}Ni_{0.67}O_y$. Notably, the highest absorption occurs in the same region that has the highest electrical conductivity (Fig. 4) and the lowest crystallinity (Fig. 2). The absorption for other wavelengths in the visible spectrum shows the same general trend—namely, that the absorption coefficient decreases for compositions with higher zinc percentages.

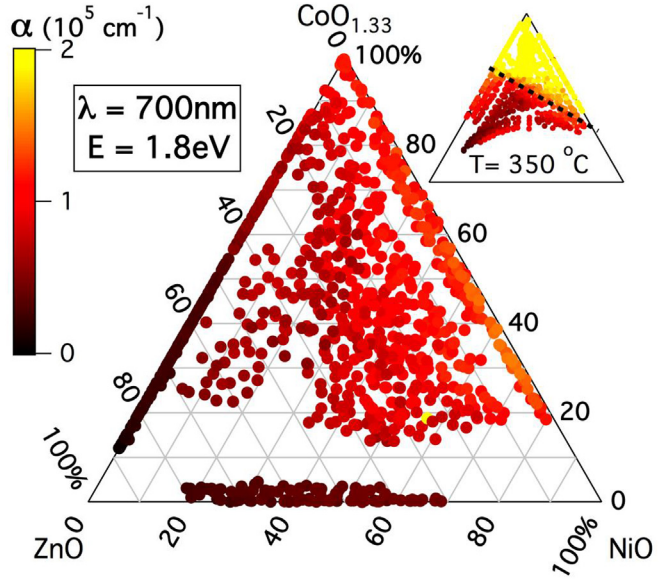

Fig. 6. Absorption coefficient (α) at $\lambda = 700$ nm vs. metal composition for ambient-temperature depositions. (Inset) Absorption coefficient for depositions at 350 °C substrate temperature [19]. The dashed line is the tie line between Co_2ZnO_4 and $CoNi_2O_4$.

For all films, the work function (see Fig. S2 in Supplemental Information) lies within the range of 5.0–5.8 eV. However, no clear trends with composition, crystal structure, or conductivity were observed. We note that the work-function measurements were done in air using a Kelvin probe on samples with no special surface treatment. Consequentially, the observed ±0.4 V variance may arise largely from spot-to-spot differences in the surface condition.

4. Discussion

Overall, the intensity of the XRD peaks measured for the ambient-temperature-deposited Co-Zn-Ni-O were much weaker than those measured for films grown at 350 °C [19], suggesting that there is likely a substantial non-crystalline or weakly crystalline component to these films. However, the composition region where a spinel structure was observed was very similar for both the films grown at ambient temperature and those grown at 350 °C. To make this clear, the spinel region boundary for films grown at $T_S = 350$ °C from Ref. [19] is shown with a solid black line in Fig. 2. Additionally, for the ambient-temperature-deposited films, a least crystalline region with no detectable XRD peaks in high-throughput mapping measurements occurs along the Co_3O_4–NiO tie line between the crystalline spinel Co_2NiO_4 and rock-salt NiO phases. As discussed above, the GIXRD measurement (Fig. 3) of this region shows the presence of at least some spinel component material, albeit with very broad and weak GIXRD peaks.

For the ambient-temperature-deposited Co-Zn-Ni-O films studied here, the maximum conductivity is 35 S/cm, which is a factor of three less than the 110 S/cm reported in Ref. [19] for films grown in the same deposition system but at $T_S = 350$ °C. Additionally, the region of highest conductivity shifted along the Co_3O_4–NiO binary tie line from Co_2NiO_4 (67% Co) for samples grown at $T_s = 350$ °C to a region along the Co_3O_4–NiO tie line with Co percentages from 30% to 50%. Higher conductivities of $\sigma = 204$ S/cm at composition Co_2NiO_4 [19] and $\sigma = 350$ S/cm at composition $Co_{1.5}Ni_{1.5}O_4$ [17] have been reported; but in both cases, the films were annealed in air at temperatures of 375 °C or higher after deposition. In both these cases and others [16], a general region of higher conductivity is observed along the Co_3NiO_4–NiO tie line for compositions Ni-rich relative to Co_2NiO_4 up to the point where NiO precipitation is observed. In this work on ambient-temperature-deposited films, we also observe increasing conductivity with increasing Ni content along the Co_3O_4–NiO tie line up to the point where NiO is observed.

Interestingly, for the ambient-temperature-deposited Co-Zn-Ni-O films studied here, the compositions with highest conductivity are also those that are the least crystalline. At this time, the specific hole-doping mechanism for these ambient-temperature-deposited materials is not known. However, we note that for crystalline Co-Ni-O, the electrical conductivity is known to depend strongly on the oxygen partial pressure during growth [8,17]. This suggests that the electrical conductivity of nano-crystalline or amorphous Co-Ni-O may be controlled by oxygen stoichiometry—as it is in n-type amorphous In-Zn-O, where the conductivity, which remains high across the compositionally broad region and is relatively independent of cation composition, but depends strongly on the oxygen partial pressure during deposition [25]. Note that here we have focused on the effects of cation composition using only one oxygen partial pressure ($pO_2 = 10$ mT) during deposition.

For a p-type oxide semiconductor, the relatively high conductivity of the Co-Zn-Ni-O films when deposited at ambient temperature is a substantial benefit for device applications [4,5,8,9,19]. This resilience of the conductivity at low deposition temperatures for the Co-Zn-Ni-O material system strongly contrasts with that observed for p-type delafossites typified by $CuAlO_2$ and $CuCrO_2$:Mg. $CuAlO_2$ has a low conductivity ($\sigma \approx 10^{-4}$ S/cm) when deposited by RF sputtering at 500 °C, and only after annealing at 900 °C does the conductivity increase to $\sigma \approx 0.1$ S/cm [20]. For $CuCrO_2$:Mg films grown by PLD, the conductivity of the films was maximized ($\sigma \approx 3$ S/cm) at a deposition temperature of 500 °C and dropped to its lowest value ($\sigma \approx 0.002$ S/cm) when the substrate was kept at room temperature [21]. For reference, the highest conductivity obtained for thin films of $CuCrO_2$:Mg is $\sigma \approx 220$ S/cm and was obtained by RF sputtering at 600 °C [26]; but no data are provided for the conductivity of $CuCrO_2$:Mg films sputtered at ambient temperature.

The absorption coefficients for the ambient-temperature-grown Co-Zn-Ni-O are similar in magnitude to those reported for films grown at $T_S = 350$ °C [19] with $\alpha \approx 1 \times 10^5$ to 4×10^5 cm^{-1} at $\lambda = 700$ nm. The high-temperature study was able to correlate changes in the absorption coefficient based on composition of the films. With a visible absorption coefficient in the 10^5 cm^{-1} range, these films are too absorbing to be used as conventional transparent contacts. However, their p-type conduction allows their use in diodes [4] and transistors [5] as well as for thin HTLs because they also have a high work function ($\phi = 5.4 \pm 0.4$ V) [8,9,19].

For the crystalline Co-Zn-Ni-O films grown at 350 °C, there is an abrupt, compositionally dependent, crossover from low absorption to strong absorption in going from the low-Co to high-Co side of the Co_2ZnO_4–$CoNi_2O_4$ tie line (Fig. 6 inset), which is attributed to optical transitions between the Co atoms in octahedral and tetrahedral positions [19]. No such clear, compositionally dependent changes in the absorption coefficient are observed for the ambient-temperature-deposited Co-Zn-Ni-O films. Rather, there is a gradual general increase in absorption coefficient with decreasing Zn content. Comparing the compositional trends for electrical conductivity (Fig. 4) and optical absorption coefficient (Fig. 6) across the full ternary composition space, there is a remarkable similarity in the overall color-scale variation, which indicates a general correlation between increasing conductivity and increasing absorption, as shown explicitly in Fig. S3 of the Supplemental Information. Further, because the conductivity is displayed with a logarithmic color scale and absorption is exponential in the absorption coefficient, there is likely to be a relatively direct correlation between sheet conductance and optical absorption in these materials.

5. Conclusions

The broad compositional dependence of the optical, electrical, and structural properties of Co-Zn-Ni-O films deposited by RF sputtering on glass at ambient temperature was investigated using high-throughput combinatorial experiments. Overall, compared to similar films grown at 350 °C, the Co-Zn-Ni-O films deposited at ambient temperature were found to: 1) be much less crystalline; 2) have a lower conductivity, with maximum conductivity being ~35 S/cm, a factor of 3 decrease; 3) have a similar-magnitude optical absorption coefficient; and 4) have a similar, and large, work function ($\phi = 5.4 \pm 0.4$ V). Notably different for the ambient-temperature-deposited films is a nearly-amorphous region observed along the Co_3O_4–NiO tie line, which is also where the electrical conductivity is highest and optical absorption strongest. Compared to other p-type oxide semiconductors, the electrical conductivity of the Co-Zn-Ni-O materials depends much less on substrate temperature, resulting in ambient-temperature-deposited films with high enough conductivity to be technologically relevant.

Acknowledgements

This work was authored in part by the National Renewable Energy Laboratory, operated by Alliance for Sustainable Energy,

LLC, for the U.S. Department of Energy (DOE) under Contract No. DE-AC36-08GO23808. This work was conducted as part of the Center for Inverse Design (CID) and the Center for Next Generation of Materials Design (CNGMD) Energy Frontier Research Centers funded by U.S. DOE, Office of Science, Basic Energy Sciences. The views expressed in the article do not necessarily represent the views of the DOE or the U.S. Government.

Appendix A. Supplementary data

Supplementary data to this article can be found online at https://doi.org/10.1016/j.jallcom.2019.05.275.

References

[1] H. Mizoguchi, M. Hirano, S. Fujitsu, T. Takeuchi, K. Ueda, H. Hosono, ZnRh2O4: a p-type semiconducting oxide with a valence band composed of a low spin state of Rh3+ in a 4d6 configuration, Appl. Phys. Lett. 80 (2002) 1207–1209.
[2] M. Dekkers, G. Rijnders, D.H.A. Blank, $ZnIr_2O_4$, a p-type transparent oxide semiconductor in the class of spinel zinc-d6-transition metal oxide, Appl. Phys. Lett. 90 (2007).
[3] S. Narushima, H. Mizoguchi, K.I. Shimizu, K. Ueda, H. Ohta, M. Hirano, T. Kamiya, H. Hosono, A p-type amorphous oxide semiconductor and room temperature fabrication of amorphous oxide p-n heterojunction diodes, Adv. Mater. 15 (2003) 1409–1413.
[4] F.L. Schein, M. Winter, T. Böntgen, H. Von Wenckstern, M. Grundmann, Highly rectifying p-ZnCo2O4/n-ZnO heterojunction diodes, Appl. Phys. Lett. 104 (2014).
[5] F.-L. Schein, H. von Wenckstern, H. Frenzel, M. Grundmann, ZnO-based n-channel junction field-effect transistor with room-temperature-fabricated amorphous p-type ZnCo2O4 gate, IEEE Electron. Device Lett. 33 (2012) 676–678.
[6] F.J. Kluepfel, F.-L. Schein, M. Lorenz, H. Frenzel, H. von Wenckstern, M. Grundmann, Comparison of ZnO-based JFET, MESFET, and MISFET, IEEE Trans. Electron Devices 60 (2013) 1828–1833.
[7] A. Zakutayev, T.R. Paudel, P.F. Ndione, J.D. Perkins, S. Lany, A. Zunger, D.S. Ginley, Cation off-stoichiometry leads to high p-type conductivity and enhanced transparency in Co2ZnO4 and Co2NiO4 thin films, Phys. Rev. B 85 (2012), 085204.
[8] P.F. Ndione, A. Garcia, N.E. Widjonarko, A.K. Sigdel, K.X. Steirer, D.C. Olson, P.A. Parilla, D.S. Ginley, N.R. Armstrong, R.E. Richards, E.L. Ratcliff, J.J. Berry, Highly-tunable nickel cobalt oxide as a low-temperature P-type contact in organic photovoltaic devices, Adv. Energy Mater. 3 (2012) 524.
[9] C.C. Mercado, A. Zakutayev, K. Zhu, C.J. Flynn, J.F. Cahoon, A.J. Nozik, Sensitized zinc cobalt oxide spinel P-type photoelectrode, J. Phys. Chem. C 118 (2014) 25340.
[10] B. Chi, J. Li, X. Yang, H. Lin, N. Wang, Electrophoretic deposition of ZnCo2O4 spinel and its electrocatalytic properties for oxygen evolution reaction, Electrochim. Acta 50 (2005) 2059–2064.
[11] M.R.G. De Chialvo, A.C. Chialvo, Oxygen evolution reaction on NixCo(3-xO4 electrodes with spinel structure, Electrochim. Acta 38 (1993) 2247–2252.
[12] P.F. Ndione, Y.Z. Shi, V. Stevanovic, A. Zakutayev, S. Lany, P.A. Parilla, J.D. Perkins, J.J. Berry, D.S. Ginley, M.F. Toney, Control of the electrical properties in spinel oxides by manipulating the cation disorder, Adv. Funct. Mater. 24 (2014) 610.
[13] J.D. Perkins, T.R. Paudel, A. Zakutayev, P.F. Ndione, P.A. Parilla, D.L. Young, S. Lany, D.S. Ginley, A. Zunger, N.H. Perry, Y. Tang, M. Grayson, T.O. Mason, J.S. Bettinger, Y.Z. Shi, M.F. Toney, Inverse design approach to hole doping in ternary oxides: enhancing p-type conductivity in cobalt oxide spinels, Phys. Rev. B 84 (2011) 205207.
[14] T.R. Paudel, A. Zakutayev, S. Lany, M. d'Avezac, A. Zunger, Doping rules and doping prototype in A_2BO_4 spinel oxides, Adv. Funct. Mater. 21 (2011) 4493–4501.
[15] C.F. Windisch, G.J. Exarhos, R.R. Owings, Vibrational spectroscopic study of the site occupancy distribution of cations in nickel cobalt oxides, J. Appl. Phys. 95 (2004) 5435–5442.
[16] D.J. Hagen, T.S. Tripathi, M. Karppinen, Atomic layer deposition of nickel-cobalt spinel thin films, Dalton Trans. 46 (2017) 4796–4805.
[17] R.R. Owings, G.J. Exarhos, C.F. Windisch, P.H. Holloway, J.G. Wen, Process enhanced polaron conductivity of infrared transparent nickel-cobalt oxide, Thin Solid Films 483 (2005) 175–184.
[18] R.R. Owings, P.H. Holloway, G.J. Exarhos, C.F. Windisch, Effect of annealing and lithium substitution on conductivity in nickel-cobalt oxide spinel films, Surf. Interface Anal. 37 (2005) 424–431.
[19] A. Zakutayev, N.E. Widjonarko, J.D. Perkins, P.A. Parilla, J.J. Berry, D.S. Ginley, Zn-Ni-Co-O wide-bandgap p-type conductive oxides with high work functions, MRS Commun. 1 (2011) 23.
[20] W. Lan, W.L. Cao, M. Zhang, X.Q. Liu, Y.Y. Wang, E.Q. Xie, H. Yan, Annealing effect on the structural, optical, and electrical properties of CuAlO2 films deposited by magnetron sputtering, J. Mater. Sci. 44 (2009) 1594–1599.
[21] T.W. Chiu, K. Tonooka, N. Kikuchi, Fabrication of ZnO and CuCrO(2): Mg thin films by pulsed laser deposition with in situ laser annealing and its application to oxide diodes, Thin Solid Films 516 (2008) 5941–5947.
[22] A. Zakutayev, N. Wunder, M. Schwarting, J.D. Perkins, R. White, K. Munch, W. Tumas, C. Phillips, An open experimental database for exploring inorganic materials, Sci. Data 5 (2018) 180053.
[23] H. Hosono, M. Yasukawa, H. Kawazoe, Novel oxide amorphous semiconductors: transparent conducting amorphous oxides, J. Non-Cryst. Solids 203 (1996) 334–344.
[24] M.P. Taylor, D.W. Readey, M.F.A.M. Van Hest, C.W. Teplin, J.L. Alleman, M.S. Dabney, L.M. Gedvilas, B.M. Keyes, B. To, J.D. Perkins, D.S. Ginley, The remarkable thermal stability of amorphous In-Zn-O transparent conductors, Adv. Funct. Mater. 18 (2008) 3169–3178.
[25] J.D. Perkins, M.F.A.M. Van Hest, M.P. Taylor, D.S. Ginley, Conductivity and transparency in amorphous In-Zn-O transparent conductors, Int. J. Nanotechnol. 6 (2009) 850–859.
[26] R. Nagarajan, A.D. Draeseke, A.W. Sleight, J. Tate, p-type conductivity in CuCr1-xMgxO2 films and powders, J. Appl. Phys. 89 (2001) 8022–8025.